Electronic Supplementary Material (ESI) for Chemical Communications.
This journal is © The Royal Society of Chemistry 2021

Electronic Supplementary Information (ESI) for:

Enhanced 5f-δ bonding in $[U(C_7H_7)_2]^-$: C K-edge XAS, magnetism and *ab initio* calculations

Yusen Qiao,[a,‡] Gaurab Ganguly,[b,‡,§] Corwin H. Booth,[a] Jacob A. Branson,[a] Alexander S. Ditter,[a] Daniel J. Lussier,[a,c] Liane M. Moreau,[a] Dominic R. Russo,[a,c] Dumitru-Claudiu Sergentu,[b] David K. Shuh,[a] Taoxiang Sun,[a] Jochen Autschbach,[b,] and Stefan G. Minasian[a,*]*

[a]Chemical Sciences Division, Lawrence Berkeley National Laboratory, Berkeley, CA 94720, USA. E-mail: sgminasian@lbl.gov
[b]Department of Chemistry, University at Buffalo, State University of New York, Buffalo, NY 14260-3000, USA. E-mail: jochena@buffalo.edu
[c] Department of Chemistry, University of California, Berkeley, CA 94720, USA.
‡ These authors contributed equally.
§ Present Address: Institute of Organic Chemistry and Biochemistry, Czech Academy of Sciences, 16610 Prague 6, Czech Republic.

E-mails: sgminasian@lbl.gov; jochena@buffalo.edu

Table of Contents:

Magnetism **S2**

STXM measurements **S3**

Computational details **S8**

Additional spectra **S11**

Isosurface Plots of all Natural Orbitals (NOs) in the Active Space and Comparison of Compositions of NOs for $[U(C_7H_7)_2]^-$, $Th(C_8H_8)_2$, and $U(C_8H_8)_2$ **S14**

References **S17**

Magnetism

Magnetic susceptibility measurements were made for all samples in a 7 T Quantum Design Magnetic Properties Measurement System that utilizes a superconducting quantum interference device (SQUID). Samples were contained in quartz tubes for measurement as described previously.[1] Data were collected at two different fields (0.5 and 4 T) and over a temperature range from 2–300 K unless otherwise stated.

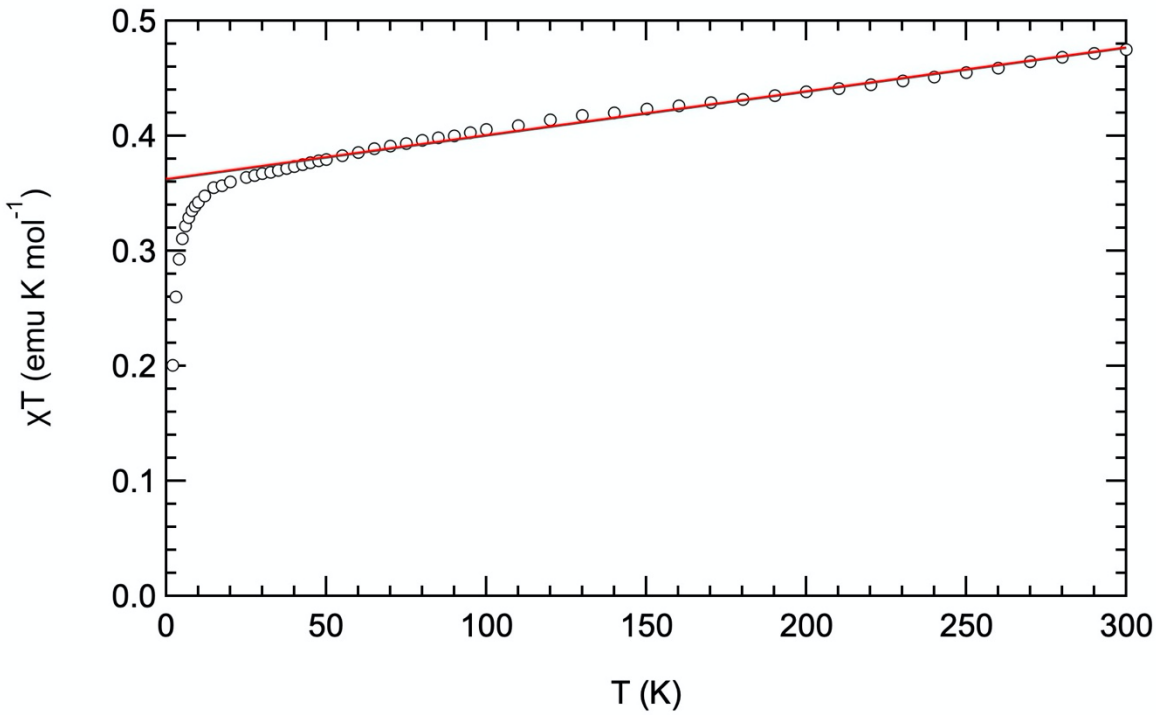

Fig. S1 Variable-temperature molar magnetic data for [K(18-crown-6)][U(C_7H_7)$_2$] and linear fit to the data from 30 K to 300 K. A two-field correction was applied in order to remove contributions from trace ferromagnetic impurities as described previously.[2] Diamagnetic corrections were made using Pascal's constants.[3]

Table S1. The molar magnetic data for [K(18-crown-6)][U(C_7H_7)$_2$] which is plotted in Fig S1.

T (K)	μ_{eff} (μ_B)	χT (emu K mol^{-1})	T (K)	μ_{eff} (μ_B)	χT (emu K mol^{-1})	T (K)	μ_{eff} (μ_B)	χT (emu K mol^{-1})
2	1.268	0.201	42.5	1.732	0.375	170.1	1.852	0.429
3	1.443	0.260	45.0	1.736	0.377	180.1	1.859	0.432
4	1.53	0.293	47.5	1.739	0.378	190.1	1.865	0.435
5	1.577	0.311	50.0	1.743	0.380	200.0	1.872	0.438
6	1.604	0.322	55.0	1.750	0.383	210.1	1.879	0.441
7	1.622	0.329	60.0	1.757	0.386	220.1	1.885	0.444
8	1.637	0.335	65.0	1.763	0.389	230.1	1.893	0.448
9	1.646	0.339	70.0	1.769	0.391	240.0	1.900	0.451
10	1.655	0.342	75.0	1.774	0.394	250.0	1.908	0.455
12	1.668	0.348	80.0	1.780	0.396	260.0	1.916	0.459
14.7	1.685	0.355	85.0	1.785	0.398	270.0	1.927	0.464
17.3	1.689	0.356	90.0	1.789	0.400	280.0	1.936	0.468
20	1.697	0.360	95.0	1.795	0.403	290.0	1.943	0.472
25	1.706	0.364	100.0	1.801	0.405	300.0	1.949	0.475
27.5	1.71	0.366	110.0	1.809	0.409			
30	1.714	0.367	120.0	1.819	0.414			
32.5	1.717	0.369	130.0	1.828	0.418			
35	1.721	0.370	139.9	1.833	0.420			
37.5	1.725	0.372	150.1	1.840	0.423			
40	1.729	0.374	160.1	1.846	0.426			

STXM Measurements

STXM sample preparation. All manipulations were performed with rigorous exclusion of air and moisture using Schlenk and glovebox techniques under an atmosphere of argon. THF was purified by passage through a column of activated alumina, degassed by passing through an argon flow, stored over sodium/benzophenone, and vacuum transferred immediately prior to use. Samples of [K(18-crown-6)][$U(C_7H_7)_2$] were prepared using the literature procedures.[4] A small amount of each sample (1 mg) was dissolved in THF (1 mL), and an aliquot of this solution (0.1 μL) was transferred to a Si_3N_4 window (100 nm, Silson) using a micropipette. The solvent was allowed to evaporate over a few seconds, which deposited thin crystallites of the sample on the Si_3N_4 membrane. After drying for several more minutes, a second window was placed over the sample, sandwiching the crystallites, and the windows were sealed together using Hardman Double/Bubble® epoxy.

STXM-XAS measurements and data analysis. The STXM methodology was similar to that discussed previously.[5] Single-energy images and carbon K-edge XAS spectra were acquired using the STXM instrument at the Advanced Light Source-Molecular Environmental Science (ALSMES) beamline 11.0.2, which is operated in top-off mode at 500 mA, in a ~0.5 atm He filled chamber.[6] An energy calibration was performed at the C K-edge for CO_2 gas (294.95 eV) and at the Ne K-edge for Ne gas (867.30 eV). For these measurements, the X-ray beam was focused with a zone plate onto the sample, and the transmitted light was detected. The spot size and spectral resolution were determined from characteristics of the 25 nm zone plate. Images at a single energy were obtained by raster-scanning the sample and collecting transmitted monochromatic light as a function of sample position. Spectra at each image pixel or particular regions of interest on the sample image were extracted from the "stack", which is a collection of images recorded at multiple, closely spaced photon energies across the absorption edge. This enabled spatial mapping of local chemical bonding information. Dwell times used to acquire an image at a single photon energy were ∼1 ms per pixel. To quantify the absorbance signal, the measured transmitted intensity (I) was converted to optical density using Beer−Lambert's law: $OD = \ln(I/I0) = \mu\rho d$, where I0 is the incident photon flux intensity, d is the sample thickness, and μ and ρ are the mass absorption coefficient and density of the sample material, respectively. Incident beam intensity was measured through the sample-free region of the Si_3N_4 windows. Spectra were then obtained by averaging over the crystallites deposited on the substrate. Regions of particles with an absorption of >1.5 OD were omitted to ensure the spectra were in the linear regime of the Beer−Lambert law. The energy resolution was determined to be 0.04 eV at the C K-edge, and spectra were collected using circularly polarized radiation. During the STXM experiment, samples showed no sign of radiation damage and each spectrum was reproduced from multiple independent crystallites. Salient features of the spectra were reproducible using samples prepared from non-oriented polycrystalline particles.

The C K-edge XAS data were normalized in MATLAB using the MBACK algorithim,[7] and by setting the edge jump at 295 eV to an intensity of 1.0. IGOR Pro 7 was used for XAS data to calculate second-derivative spectra which were used as guides to determine the number and position of peaks.

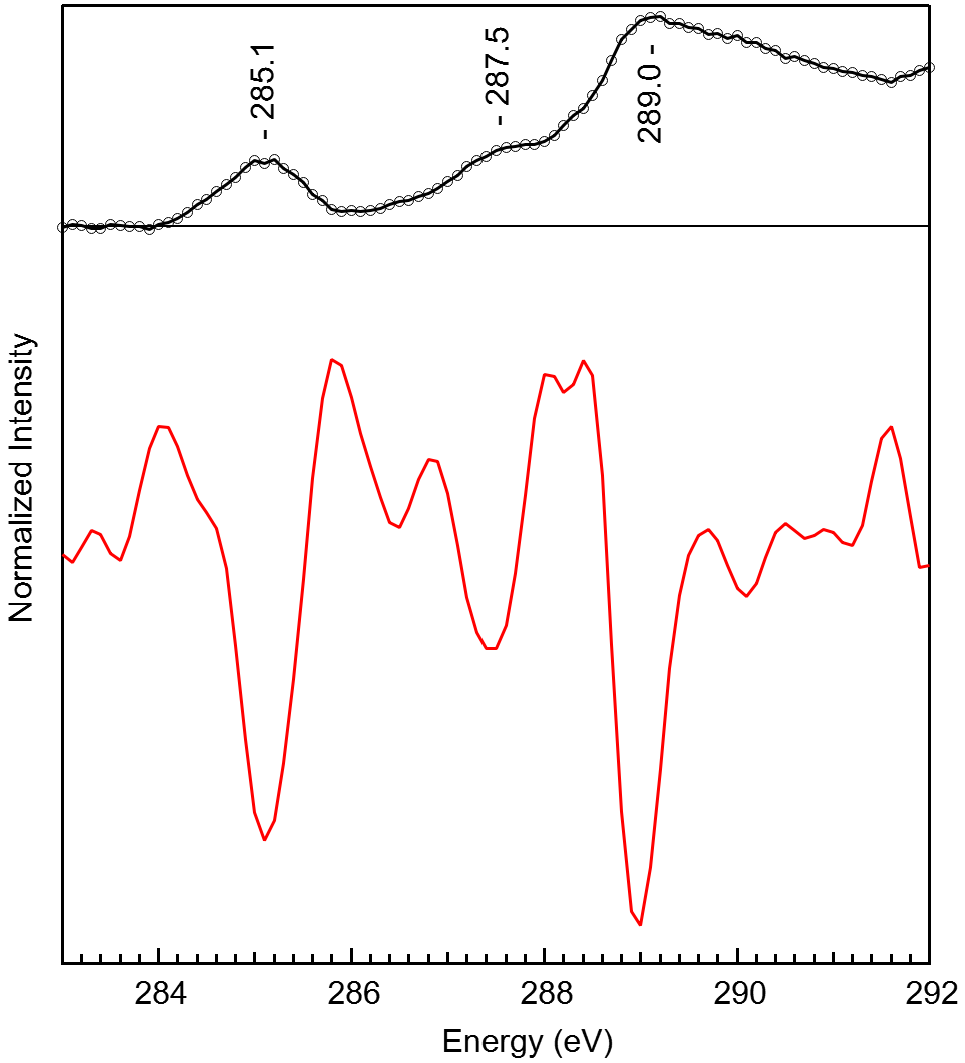

Fig. S2. Experimental C K-edge XAS of [K(18-crown-6)][U(C_7H_7)$_2$] (black circles) with 2nd derivative of the data (red). Energies of the C K-edge XAS features are provided and were determined using the minimum of the 2nd derivative.

Table S2. Normalized C K-edge XAS data of [K(18-crown-6)][U(C_7H_7)$_2$].

Energy	Normalized Intensity
275	-0.003683095563852237
276	0.004483353430883751
277	0.002253153212902627
278	-0.002357836189504441
279	-0.006125620666465692
280	-0.001299811724601721
280.5	0.002546735152934629
281	0.003309958490828561
281.5	0.00409177816942235
282	0.003135288593094172
282.5	0.001208314658071099
283	-0.004069156830461703
283.1	0.012656560304246

283.2	0.005746729123669503
283.3	-0.01092247941933539
283.4	-0.01348783456624075
283.5	0.01223720729077291
283.6	0.005548851656888436
283.7	-0.001051235605129513
283.8	0.002859633374301417
283.9	-0.0171407265264476
284	0.01411610277578091
284.1	0.02492937643484916
284.2	0.05468251745008464
284.3	0.09871915914940983
284.4	0.1492981123762261
284.5	0.1837472323354127
284.6	0.2355686292697632
284.7	0.2874649259096074
284.8	0.3330932217146302
284.9	0.4009211325742643
285	0.4509507455418222
285.1	0.4303755072699024
285.2	0.4526656076803562
285.3	0.3963701736892145
285.4	0.3510749715928855
285.5	0.2997110590636087
285.6	0.2154683046170257
285.7	0.177801222085662
285.8	0.1182506597407416
285.9	0.1032552164738075
286	0.1069476427892308
286.1	0.1005231825244069
286.2	0.1122745634580154
286.3	0.1228649630127774
286.4	0.1529617211232985
286.5	0.1704641421051411
286.6	0.1784806831621177
286.7	0.2051354961389514
286.8	0.2231898661966932
286.9	0.2572987037079981
287	0.3029592560814415
287.1	0.3477361500823227
287.2	0.4102982167288918
287.3	0.4482977297497855
287.4	0.4787839204137003
287.5	0.5152871321568536
287.6	0.5367461679382232
287.7	0.5403408853743942
287.8	0.5583169538297428
287.9	0.5538834032882685
288	0.5764973911833592
288.1	0.6172116967743432
288.2	0.6887720473992998
288.3	0.7534201702107924
288.4	0.7982393618254761

288.5	0.8919983999257936
288.6	0.9941629524847528
288.7	1.126152656355077
288.8	1.268139160076989
288.9	1.335711406905828
289	1.398662987268975
289.1	1.417431672193493
289.2	1.423645548779074
289.3	1.379772395241519
289.4	1.376801729935301
289.5	1.349878324791874
289.6	1.340720497182478
289.7	1.305074994782367
289.8	1.308849453887716
289.9	1.278891310901375
290	1.294947406256522
290.1	1.249524082276279
290.2	1.247063237715372
290.3	1.205564362405213
290.4	1.193813510191777
290.5	1.142848943719129
290.6	1.152184425944392
290.7	1.123632748185423
290.8	1.10777520116875
290.9	1.07815845372539
291	1.072970874011548
291.1	1.054646429979361
291.2	1.048335482225263
291.3	1.027444519166106
291.4	1.014881223477031
291.5	0.9969860399322867
291.6	0.9772888945574287
291.7	1.01982654268024
291.8	1.024135983118058
291.9	1.05563731651323
292	1.080525125802936
292.5	1.117098114695174
293	1.163207499478237
293.5	1.217829789207616
294	1.232882243814206
294.5	1.208810472369733
295	1.200852677225611
295.5	1.193290680147485
296	1.167091528882499
296.5	1.184913990214039
297	1.223490874939128
297.5	1.246183892586323
298	1.190626046425342
298.5	1.162271270551678
299	1.186772302483593
299.5	1.220530273867774
300	1.269082809637548
300.5	1.193035433527352

301	1.171995895461819
301.5	1.118156923219628
302	1.119476543839714
304	1.064642928367692
306	1.022390325348422
308	0.9964560907172506
310	0.9720151891102197
312	0.9578583818379982
314	0.9466126660946594
316	0.9202476404702826
318	0.8957088328734086
320	0.8895100990190848
322	0.8695172181898291
324	0.849026111355889
326	0.8271492475013333
328	0.8141340120121512
330	0.7855518864642997
332	0.7753070287317674
334	0.7601407369617141
336	0.7540264128191453
338	0.7382427474897386
340	0.7362350022030008
345	0.7165858358648517
350	0.6886823504858196
355	0.6829870834589431
360	0.6437113373373837
365	0.6214666187417388
370	0.6053304269183498
375	0.5788959024186628
380	0.5838139276024396

Computational details

Details of Kohn-Sham Theory (KST) Calculations. The molecular structure for the $[U(C_7H_7)_2]^-$ complex, with D_{7d} symmetry (staggered conformation), was obtained by averaging the experimental crystal structure data for the U–C and C–C metrics, followed by optimization of the hydrogen positions with Kohn-Sham density functional theory (KST). These calculations employed the scalar relativistic (SR) zeroth-order regular approximation (ZORA) Hamiltonian,[8] the Becke-Perdew (BP) generalized gradient approximation (GGA) exchange-correlation functional,[9] and all-electron doubly-polarized triple-ζ (TZ2P) Slater-type basis sets.[10] The 2019.3 release of the Amsterdam Density Functional (ADF) program package[11] was used for KST calculations. The two $(C_7H_7)^{3-}$ ligands (henceforth alternatively referred to as Ch ligands, with charges implied) are perpendicular to the C_7 principal rotation axis (aligned with the Cartesian *z*-axis) connecting the ring centroids and the U atom. This averaged experimental structure and was used for the subsequent multireference wave function and KST calculations of the C K-edge X-ray absorption near-edge structure (XANES) spectra. Note that the eclipsed and staggered conformers of $[U(C_7H_7)_2]^-$ are essentially iso-energetic and share similar electronic structure and metal-ligand bonding.[12]

The C K edge intensities of the full complex, i.e. $[K(18\text{-crown-}6)][U(C_7H_7)_2]$, were calculated using the crystal structure coordinates, with hydrogen positions optimized, with unrestricted KST and the PBE approximation,[13] the SR-ZORA all-electron Hamiltonian,[8] and TZ2P basis sets[10] for all atoms. Additionally, the C K edge XANES was calculated for the averaged experimental structure of the $[U(C_7H_7)_2]^-$ complex ion, using the full D_{7d} symmetry, both the SR- and spin-orbit (SO)-ZORA Hamiltonians, various common KST approximations such as the PBE GGA, the B3LYP hybrid GGA,[14] the asymptotically correct SAOP potential,[15] and TZ2P basis sets for all atoms.

Details of Wavefunction Theory (WFT) Calculations. The Restricted Active Space (RAS) Self Consistent Field (SCF) approach, a restricted variant of the Complete Active Space (CAS) SCF method,[16] was used to generate 'spin-free' (SF) multiconfigurational wavefunctions belonging to a given spin multiplicity. In a typical RAS calculation, a chosen set of molecular orbitals, used as a one-particle basis to generate configurations (active space), is partitioned into three subspaces, RAS1/2/3. The possible configurations for a configurational interaction (CI) are generated through a pre-selected maximum number of holes/electrons in RAS1/3, while RAS2 is unrestricted. For C K-edge XANES, the C 1s core-orbitals span RAS1, with one hole allowed, while the valence orbitals are partitioned into RAS2/3. A post-SCF multiconfiguration pair-density functional theory (MC-pDFT), with the 'translated' tLSDA or tPBE functional[17] was used to recover the dynamic correlation. The performance of the MC-pDFT approximations in predicting valence excited state (ES) energies was benchmarked against multistate second-order RAS perturbation theory (PT2) energies, to infer the applicability of MC-pDFT for the core-ESs (see Table S3 and S4). Scalar relativistic (SR) effects in the SF wavefunction calculations were included via the second-order Douglas-Kroll-Hess (DKH2) Hamiltonian[8, 18] in combination with all-electron atomic natural orbital-relativistically contracted polarized valence triple-ζ basis sets (ANO-RCC-VTZP).[19] SO coupling was treated by state-interaction of different spin states (RASSI), using an atomic mean-field approximation for the SO integrals (AMFI).[20] In this report, tLSDA/tPBE-SO designations are used when the diagonal elements of the SO Hamiltonian were 'dressed' with tLSDA/tPBE energies. The RASSI module was also used to calculate the electric-dipole intensities between the ground state (GS) and various core-ESs, which were subsequently used to produce C K-edge XANES spectra. Due to the lack of support for the non-abelian D_{7d} point group symmetry in Molcas, the calculations were performed within the C_i abelian subgroup, preserving the molecular inversion symmetry such that U 5f and 6d basis orbitals span different parity, *ungerade* (*u*) and *gerade* (*g*), respectively. Spurious mixing among same-symmetry orbitals in C_i that would not be allowed in the parent D_{7d} point group was suppressed by employing the 'supersymmetry' capabilities of Molcas.

Details for RAS Partition for XANES Calculations. A detailed assignment of the pre- and rising-edge features in the spectrum that are due to the transitions within the $[U(C_7H_7)_2]^-$ moiety can be made with the help of the wavefunction calculations. The frontier orbitals for a hypothetical $(C_7H_7)_2^{6-}$ fragment (i.e., Ch_2

in our abbreviated notation) in $[U(C_7H_7)_2]^-$ resemble the frontier orbitals for a hypothetical $(C_8H_8)_2^{4-}$ fragment in uranocene ($U(C_8H_8)_2$), as each of the aryl systems is 10π Hückel aromatic and the dimer has 20π electrons in each case. In a recent study, we showed that the C K-edge XANES for a hypothetical $(C_8H_8)_2^{4-}$ fragment gives one single electric-dipole allowed intense transition, polarized along the principal symmetry axis (||-axis).[21] Likewise, the dominant intensity of the C K-edge XANES of $[U(C_7H_7)_2]^-$ is expected to be gained via C 1s core excitations into empty Ch FOs derived mainly from C 2p, namely ϕ_u, ϕ_u^* and ϕ_g. Then, in the C K edge XANES, the extent of metal-ligand orbital mixing may identify with the occurrence of distinct pre-edge features, generated by core excitations into valence orbitals of mixed U 5f/6d and C 2p character XANES, the extent of metal-ligand orbital mixing may identify with the occurrence of distinct pre-edge features, generated by core excitations into valence orbitals of mixed U 5f/6d and C 2p character.

In the XANES calculations, two different active spaces were explored. The first active space considered the C 1s orbitals with at most one hole in RAS1, the U-centered σ_u singly-occupied valence MO in RAS2, and the δ_u^*, p_g^*, ϕ_u, ϕ_u^* and ϕ_g MOs, in RAS3 with one electron occupation allowed. A single valence state was calculated (i.e. the GS), while all possible core ESs of *g* symmetry were calculated (because only these core ESs are electric dipole allowed from the *u* symmetry GS). In these calculations, the GS orbital-mixing of the active space orbitals was preserved with supersymmetry designations. This constraint was necessary to restrict valence orbital rotation out of the active space. The spectrum obtained with KST (Fig. S4), agree with the spectra obtained with MC-pDFT, with tLSDA and tPBE (Fig. S5) in terms of spectral features. However, in both the calculated MC-pDFT and the KST XANES spectra, the energy splitting between the pre-edge peak and the rising edge is underestimated, much likely due to constraining the orbital hybridization in the core excited states and/or since additional valence orbitals were not accounted for in the active space.

The second active space which is used in the main paper is described as follows. Fourteen C 1s cores with 28 electrons comprised the RAS1 partition, with one hole allowed. RAS2 partition consisted of seven metal-centered $\sigma_u/\pi_u/\delta_u^*/\phi_u$ orbitals. Additionally, two pairs of ϕ-symmetry ligand-centered orbitals, both ϕ_u^* and ϕ_g, with one particle allowed constituted the RAS3 partition to account for the main ligand-centered C 1s core to C 2p based excitations. In terms of orbital re-hybridization in the generated valence and core ESs, ϕ_u and ϕ_u^* could mix in supersymmetry, while the remaining MOs in the active space were constrained to be the same as in the GS. Again, these constraints were necessary to preserve the active space. It is important to note that the natural orbitals (NOs) generated for the ES wavefunctions exhibit pronounced differences with respect to the GS NOs, as these orbitals mix in the same supersymmetry. The corresponding active space is denoted as RAS(28,14|1,7|0,4). The chosen RAS partition generates 735 spin-doublets ($S = 1/2$) and 343 spin-quartets ($S = 3/2$) in *g* symmetry for the core-ESs depending upon the spin pairing between the core-hole (C $1s^{27}$, in RAS1) and target $[\sigma_u / \pi_u / \delta_u^* / \phi_u / \phi_u^* / \phi_g]^2$ configurations (in RAS2/3), which mix via SO coupling to generate multiplet structure. All core-ESs (doublets and quartets) in *g* symmetry were calculated for the chosen active space, however, only 7 spin-doublets ($S = 1/2$) were calculated in for the valence excited states in *u* symmetry. All SF states, calculated in the RAS step, were considered in subsequent MC-pDFT (with tLSDA functional) and SO calculations. The C K edge spectrum obtained with this active space setup (see Figure 4 of the main article) shows excellent agreement with the experimental spectrum not only in terms of spectral features and their relative intensity (by considering that the cryptand contributions to the rising edge are not included) but also in terms of peak energy splitting. Therefore, this spectrum and the underlying ESs were used for detailed analysis in the main article.

Table S2 and S3 characterizes various low-energy SF and SO states calculated with different active spaces. In a minimal active space CAS (1,7) calculation (only metal-centered orbitals, Table S2), gives rise to similar LF energies and similar composition of the SO states when compared with CAS(5,11) calculation (active space with two doubly occupied ligand-centered δ_u orbitals, Table S3). Hence, we infer that the calculated spectrum is not sensitive to leaving the δ_u orbitals out of the active space. The assignment of the intense core-ESs in the main paper was therefore conducted without δ_u orbitals in the active space which results in a cleaner spectrum and likewise opens the possibility of much straightforward analysis. However,

ab initio XANES spectrum with tLSDA-SO with the inclusion of ligand-centered δ_u orbitals in the active space was also calculated. The corresponding active space is denoted as RAS(32,16|1,7|0,4) and only core-ESs were calculated. The chosen RAS partition generates 27,447 spin-doublets (S = 1/2 and 20,374 spin-quartets (S = 3/2) in g symmetry for the core-ESs depending upon the spin pairing between the core-hole ((C-1s δ_u)^{31}, in RAS1) and target $[\sigma_u / \pi_u / \delta_u^* / \phi_u / \phi_u^* / \phi_g]^2$ configurations (in RAS2/3), however, only 359 spin-doublet and 182 spin-quartet core-ES were calculated in the RAS SCF, MC-pDFT (tLSDA), and subsequent tLSDA-SO step to generate multiplet structure. The corresponding XANES spectrum is shown in Fig. S6

Table S3 GS and Low-lying Valence ESs for $[U(C_7H_7)_2]^-$ with CAS(1,7): SF States are Arranged in Terms of Increasing CAS Energy. Occupations of the Active-Space NOs for SF States are Given. Compositions of the SO States are Given in Terms of the SF States. Performance of tLSDA-(SO) is Compared Against PT2-(SO).

CAS(1,7)-SF					CAS(1,7)-SO			
		ΔE				ΔE		
SF-State	Configuration	CAS	PT2	tLSDA	Comp. (%SF)[a]	CAS	PT2	tLSDA
$^2\Sigma_u$	$(\sigma_u)^{1.00}(\pi_u)^{0.00}(\phi_u)^{0.00}(\delta_u^*)^{0.00}$	0.00	0.00	0.00	70%$^2\Sigma_u$ + 30%$^2\Pi_u$	0.00	0.00	0.00
$^2\Phi_u$	$(\sigma_u)^{0.00}(\pi_u)^{0.00}(\phi_u)^{1.00}(\delta_u^*)^{0.00}$	0.30	0.37	0.45	100%$^2\Phi_u$	0.16	0.26	0.33
$^2\Pi_u$	$(\sigma_u)^{0.00}(\pi_u)^{1.00}(\phi_u)^{0.00}(\delta_u^*)^{0.00}$	0.53	0.49	0.52	91%$^2\Pi_u$ + 9%$^2\Delta_u$	0.81	0.83	0.85
$^2\Delta_u$	$(\sigma_u)^{0.00}(\pi_u)^{0.00}(\phi_u)^{0.00}(\delta_u^*)^{1.00}$	1.91	2.55	2.46	70%$^2\Pi_u$ + 30%$^2\Sigma_u$	0.93	0.91	0.92
					100%$^2\Phi_u$	0.93	1.02	1.09
					91%$^2\Delta_u$ + 9%$^2\Pi_u$	2.08	2.69	2.60
					100%$^2\Delta_u$	2.44	3.08	3.00

[a]Composition of SO states are given in terms of weight-% of the SF-states provided in the first column.

Table S4 GS and low-lying valence ESs for $[U(C_7H_7)_2]^-$ obtained with CAS(5,11)SCF. Occupations of the active-space natural orbitals (NOs) for the SF states are given. Compositions of the SO states are given in terms of the SF states.[a]

CAS(5,11)-SF					CAS(5,11)-SO			
		ΔE				ΔE		
SF-state	Configuration	CAS	PT2	tLSDA	Comp. (% SF)[b]	CAS	PT2	tLSDA
$^2\Sigma_u$	$(\delta_u)^{3.72}(\sigma_u)^{0.99}(\pi_u)^{0.02}(\phi_u)^{0.02}(\delta_u^*)^{0.24}(\phi_u^*)^{0.01}$	0.00	0.00	0.00	71%$^2\Sigma_u$ + 30%$^2\Pi_u$	0.00	0.00	0.00
$^2\Phi_u$	$(\delta_u)^{3.74}(\sigma_u)^{0.01}(\pi_u)^{0.01}(\phi_u)^{0.98}(\delta_u^*)^{0.24}(\phi_u^*)^{0.02}$	0.21	0.47	0.48	100%$^2\Phi_u$	0.13	0.40	0.37
$^2\Pi_u$	$(\delta_u)^{3.69}(\sigma_u)^{0.05}(\pi_u)^{0.99}(\phi_u)^{0.03}(\delta_u^*)^{0.24}(\phi_u^*)^{0.00}$	0.50	0.50	0.57	100%$^2\Pi_u$	0.81	0.93	0.86
$^2LMCT_u$[c]	$(\delta_u)^{2.96}(\sigma_u)^{0.99}(\pi_u)^{0.01}(\phi_u)^{0.98}(\delta_u^*)^{0.05}(\phi_u^*)^{0.01}$	1.72	1.75	1.50	71%$^2\Pi_u$ + 30%$^2\Sigma_u$	0.86	0.95	0.97
$^2\Delta_u$	$(\delta_u)^{3.51}(\sigma_u)^{0.08}(\pi_u)^{0.26}(\phi_u)^{0.19}(\delta_u^*)^{0.95}(\phi_u^*)^{0.01}$	1.86	1.90	1.89	100%$^2\Phi_u$	0.94	1.11	1.11
					100%$^2LMCT_u$	1.82	1.84	1.56
					100%$^2LMCT_u$	2.09	2.24	1.97
					100%$^2\Delta_u$	2.23	2.26	2.10
					100%$^2\Delta_u$	2.34	2.38	2.35

[a]tPBE and tLSDA calculations provided similar results and therefore only tLSDA data are listed. [b]Composition of SO states are given in terms of weight-% of the SF-states provided in the first column. [c]$LMCT_u$ denotes a ligand-to-metal charge transfer state.

Additional XANES Spectra

Additional XANES Spectra Calculated with Kohn-Sham Theory

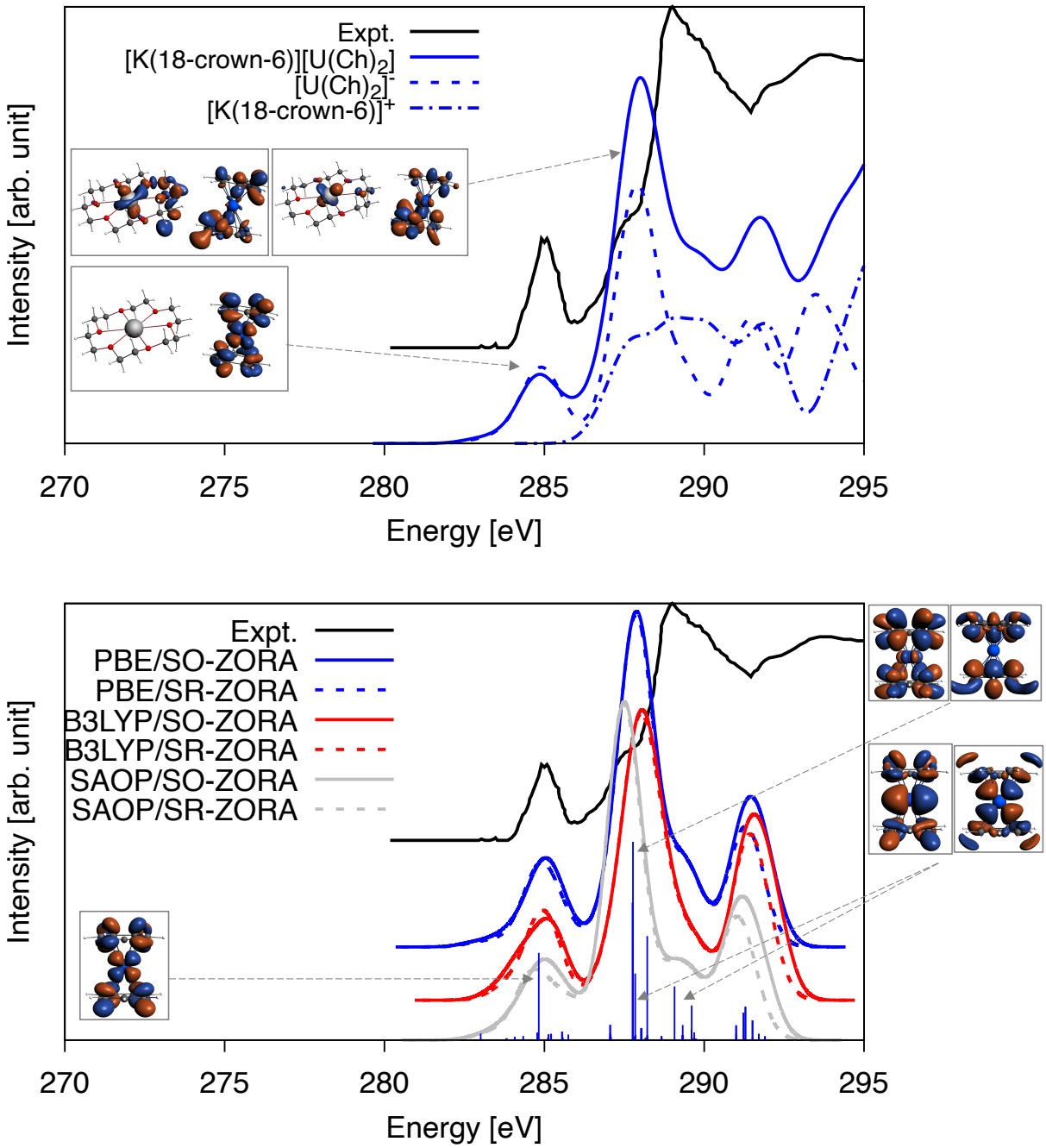

Fig. S3 Calculated C K edge XANES for [K(18-crown-6)][U(C_7H_7)$_2$] full complex (top, KST/PBE) and D_{7d} [U(C_7H_7)$_2$]$^-$ complex ion (bottom, various KST approximations). For the complex ion, the KST/PBE stick spectrum is also shown. Selected acceptor KS/PBE orbitals which contribute to intense core ESs of the first (pre-edge) and main peak are shown as ±0.03 a.u. isosurfaces. For the full complex, the KST/PBE spectrum is blue-shifted by 17.1 eV to match the energy of the first peak in the experimental spectrum. Likewise, the calculated spectrum for the complex ion was blue-shifted by 17.1 eV (PBE), 8.5 eV (B3LYP) and 16.5 eV (SAOP). All the calculated spectra were generated with a 0.5 eV Gaussian broadening of the individual transitions.

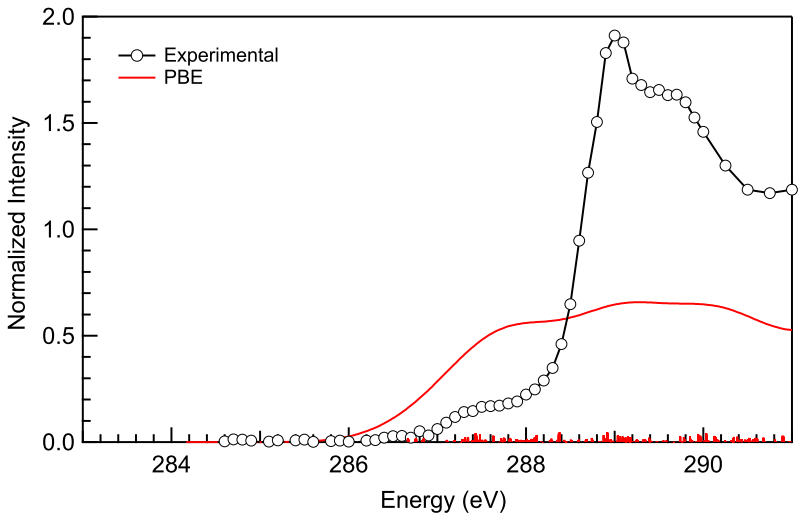

Fig. S4. Experimental C K-edge XAS for [K(18-crown-6)]Br, black, compared with the calculated spectrum for [K(18-crown-6)]$^{1+}$ (red).

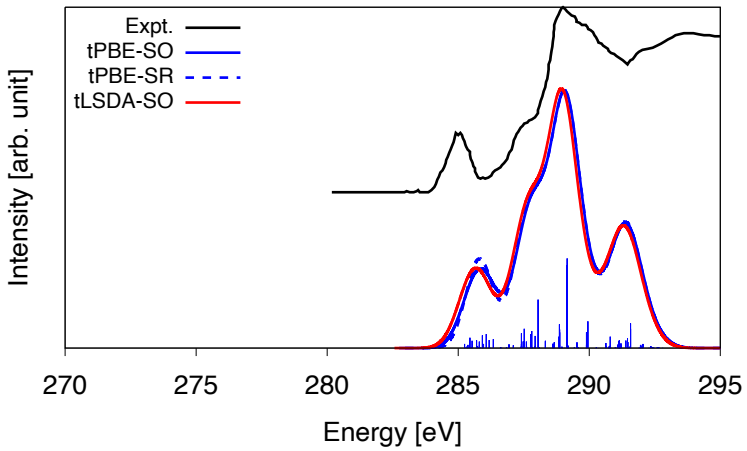

Fig. S5 Calculated vs. experimental C K-edge spectrum of $[U(C_7H_7)_2]^-$. The tLSDA-SO and tPBE-SO spectra was blue-shifted by 7.2 and 4 eV respectively, to match the position of the first peak in the experimental spectrum and generated with a 0.5 Gaussian broadening for the individual transitions. Intensities of individual transitions are shown with underlying 'stick spectra' obtained with tPBE-SO.

Additional XANES Spectra Calculated with Wavefunction Theory

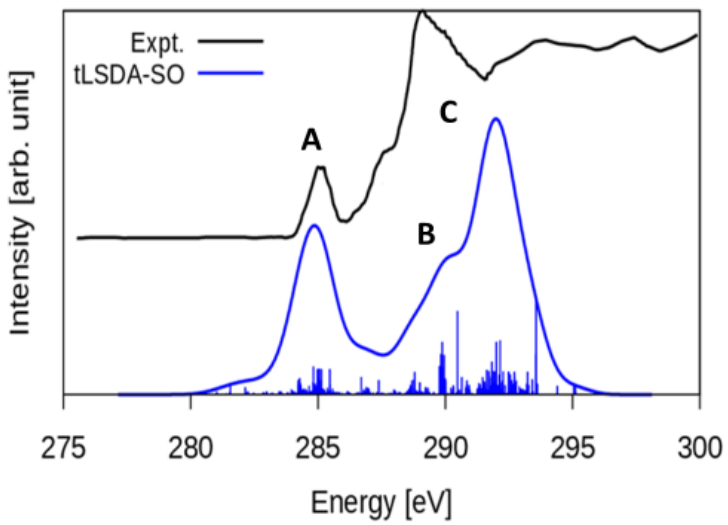

Fig. S6 Calculated vs. experimental C K-edge spectrum of $[U(C_7H_7)_2]^-$. The MC-pDFT/tLSDA-SO spectrum was blue-shifted by 12.8 eV to match the position of the first peak in the experimental spectrum. Intensities of individual transitions are shown with underlying 'stick spectra' obtained with tLSDA-SO.

Isosurface Plots of all Natural Orbitals (NOs) in the Active Space and Comparison of Compositions of NOs for $[U(C_7H_7)_2]^-$, $Th(C_8H_8)_2$, and $U(C_8H_8)_2$

1. $[U(C_7H_7)_2]^-$:

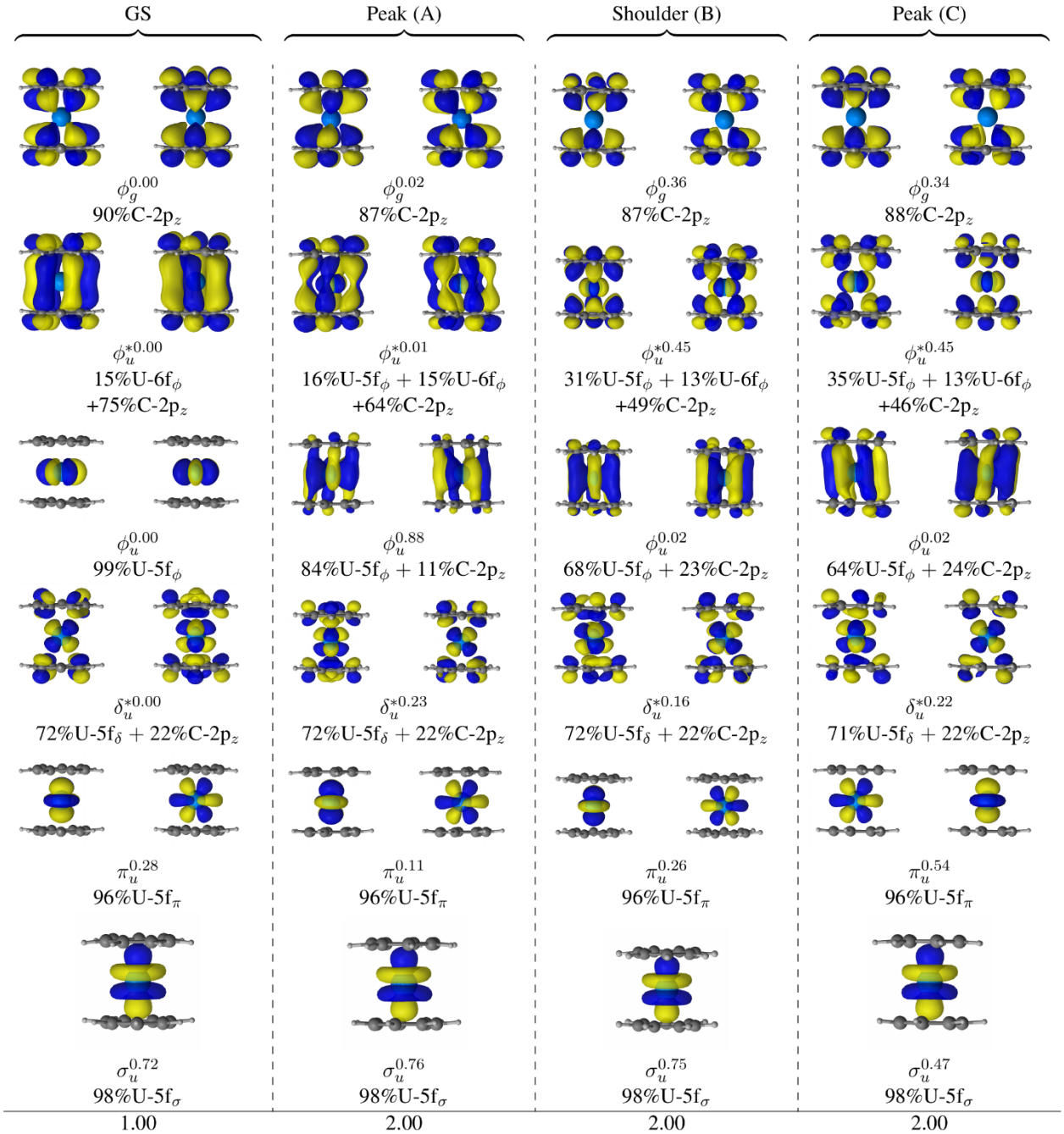

Fig. S7 $[U(C_7H_7)_2]^-$: Natural orbital (NO) isosurfaces (±0.03) and occupations extracted from the tLSDA-SO wavefunction of the GS, most intense core-ES of the first peak, the second most intense peak and its preceding shoulder with U 5f and C $2p_z$ weight-% compositions (combined weights) of the corresponding NOs. The bottom row shows the population sum of the valence NOs.

a) $Th(C_8H_8)_2$:

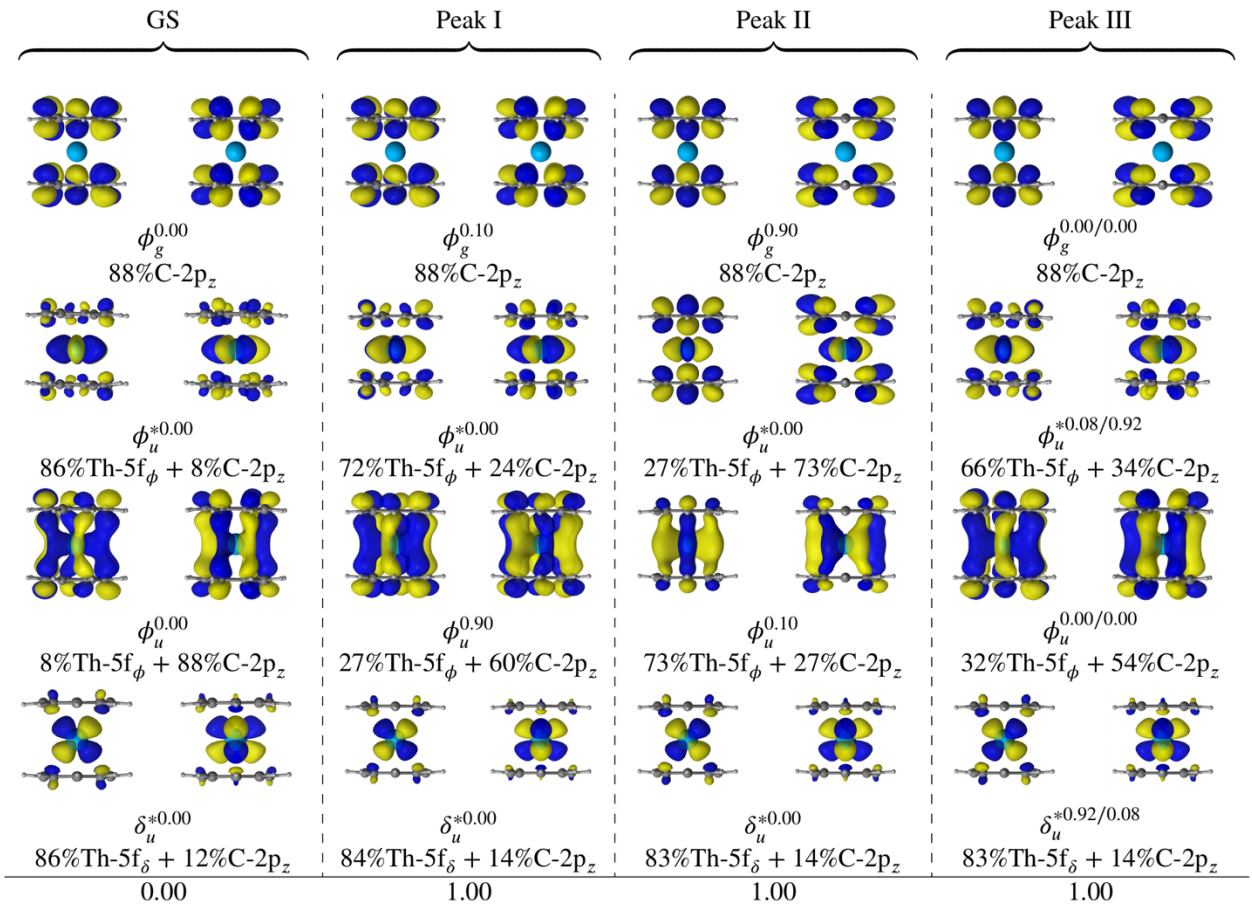

Fig. S8 $Th(C_8H_8)_2$: Natural orbital (NO) isosurfaces (±0.03) and occupations extracted from the PT2-SO wavefunction of the GS, and most intense core-ES of the first, the second, and the third most intense peak with Th 5f and C $2p_z$ weight-% compositions (combined weights) of the corresponding NOs shown in Ref 23. The bottom row shows the population sum of the valence NOs.

b) $U(C_8H_8)_2$:

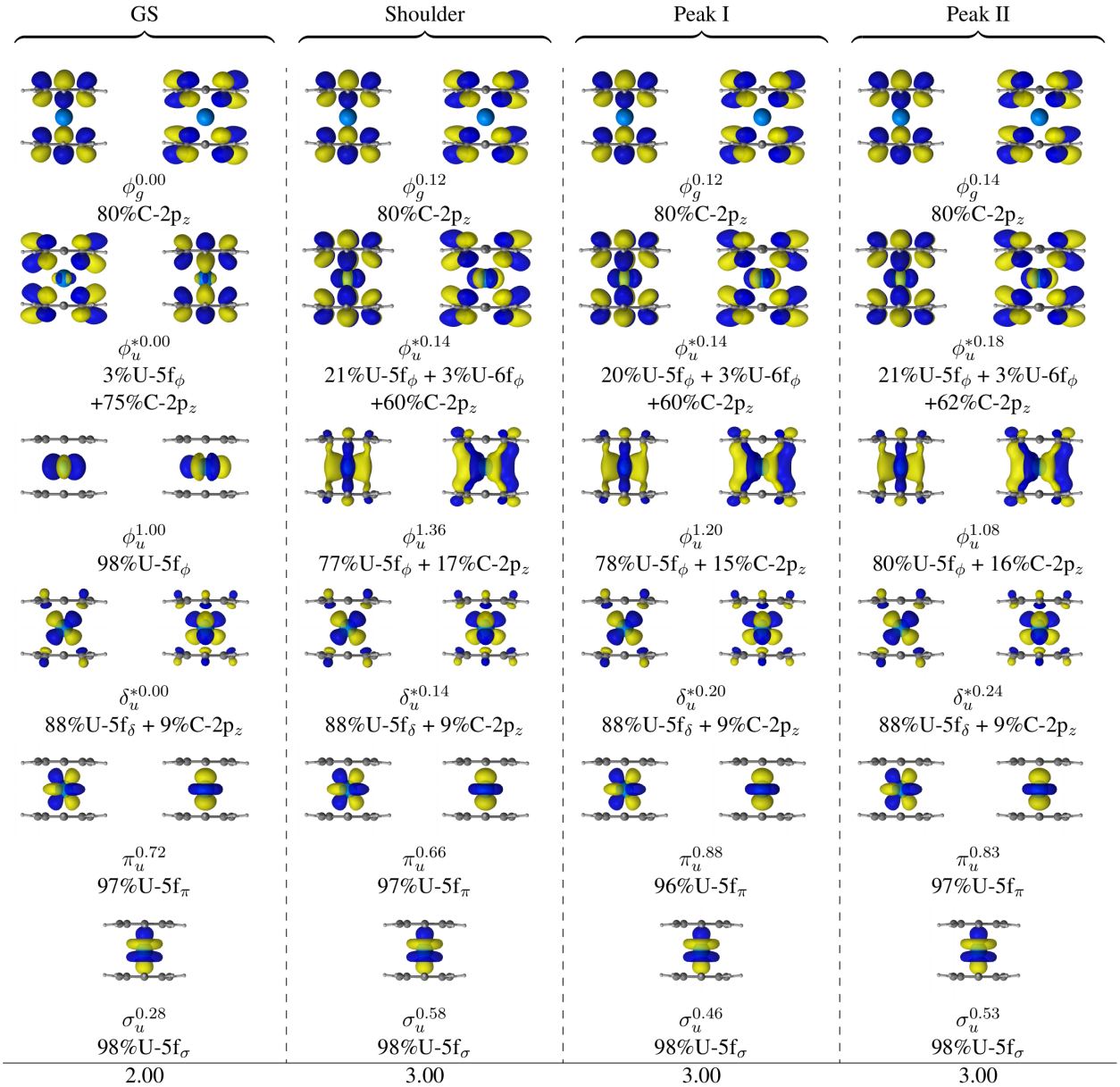

Fig. S9 $U(C_8H_8)_2$: Natural orbital (NO) isosurfaces (±0.03) and occupations extracted from the PT2-SO wavefunction of the GS, and most intense core-ES of the shoulder, the first, and the second most intense peak with U 5f and C 2p$_z$ weight-% compositions (combined weights) of the corresponding NOs shown in Ref 23. The bottom row shows the population sum of the valence NOs.

References

1. M. D. Walter, M. Schultz and R. A. Andersen, *New J. Chem.*, 2006, **30**, 238-246.
2. R. L. Halbach, G. Nocton, C. H. Booth, L. Maron and R. A. Andersen, *Inorg. Chem.*, 2018, **57**, 7290-7298.
3. G. A. Bain and J. F. Berry, *J. Chem. Educ.*, 2008, **85**, 532.
4. T. Arliguie, M. Lance, M. Nierlich, J. Vigner and M. Ephritikhine, *J. Chem. Soc., Chem. Commun.*, 1995, 183-184.
5. (a) M. W. Löble, J. M. Keith, A. B. Altman, S. C. E. Stieber, E. R. Batista, K. S. Boland, S. D. Conradson, D. L. Clark, J. Lezama Pacheco, S. A. Kozimor, R. L. Martin, S. G. Minasian, A. C. Olson, B. L. Scott, D. K. Shuh, T. Tyliszczak, M. P. Wilkerson and R. A. Zehnder, *J. Am. Chem. Soc.*, 2015, **137**, 2506-2523; (b) S. G. Minasian, J. M. Keith, E. R. Batista, K. S. Boland, D. L. Clark, S. A. Kozimor, R. L. Martin, D. K. Shuh and T. Tyliszczak, *Chem. Sci.*, 2014, **5**, 351-359; (c) S. G. Minasian, J. M. Keith, E. R. Batista, K. S. Boland, S. A. Kozimor, R. L. Martin, D. K. Shuh, T. Tyliszczak and L. J. Vernon, *J. Am. Chem. Soc.*, 2013, **135**, 14731-14740.
6. H. Bluhm, K. Andersson, T. Araki, K. Benzerara, G. E. Brown, J. J. Dynes, S. Ghosal, M. K. Gilles, H. C. Hansen, J. C. Hemminger, A. P. Hitchcock, G. Ketteler, A. L. D. Kilcoyne, E. Kneedler, J. R. Lawrence, G. G. Leppard, J. Majzlam, B. S. Mun, S. C. B. Myneni, A. Nilsson, H. Ogasawara, D. F. Ogletree, K. Pecher, M. Salmeron, D. K. Shuh, B. Tonner, T. Tyliszczak, T. Warwick and T. H. Yoon, *J. Electron Spectrosc. Relat. Phenom.*, 2006, **150**, 86-104.
7. T. C. Weng, G. S. Waldo and J. E. Penner-Hahn, *J. Synchrotron Rad.*, 2005, **12**, 506-510.
8. (a) E. v. Lenthe, E. J. Baerends and J. G. Snijders, *J. Chem. Phys.*, 1993, **99**, 4597-4610; (b) E. van Lenthe, A. Ehlers and E.-J. Baerends, *J. Chem. Phys.*, 1999, **110**, 8943-8953.
9. (a) J. P. Perdew, *Physical Review B*, 1986, **33**, 8822-8824; (b) A. D. Becke, *Phys. Rev. A*, 1988, **38**, 3098-3100.
10. E. Van Lenthe and E. J. Baerends, *J. Comput. Chem.*, 2003, **24**, 1142-1156.
11. (a) G. te Velde, F. M. Bickelhaupt, E. J. Baerends, C. Fonseca Guerra, S. J. A. van Gisbergen, J. G. Snijders and T. Ziegler, *J. Comput. Chem.*, 2001, **22**, 931-967; (b) E. J. Baerends, T. Ziegler, A. J. Atkins, J. Autschbach, O. Baseggio, D. Bashford, A. Bérces, F. M. Bickelhaupt, C. Bo, P. M. Boerrigter, L. Cavallo, C. Daul, D. P. Chong, D. V. Chulhai, L. Deng, R. M. Dickson, J. M. Dieterich, D. E. Ellis, M. van Faassen, L. Fan, T. H. Fischer, A. Förster, C. F. Guerra, M. Franchini, A. Ghy- sels, A. Giammona, S. J. A. van Gisbergen, A. Goez, A. W. Götz, J. A. Groeneveld, O. V. Gritsenko, M. Grüning, S. Gusarov, F. E. Harris, P. van den Hoek, Z. Hu, C. R. Jacob, H. Jacobsen, L. Jensen, L. Joubert, J. W. Kaminski, G. van Kessel, C. König, F. Kootstra, A. Kovalenko, M. V. Krykunov, E. van Lenthe, D. A. McCor- mack, A. Michalak, M. Mitoraj, S. Morton, J. Neugebauer, V. P. Nicu, L. Noodle- man, V. P. Osinga, S. Patchkovskii, M. Pavanello, C. A. Peeples, P. H. T. Philipsen, D. Post, C. C. Pye, H. Ramanantoanina, P. Ramos, W. Ravenek, J. I. Rodríguez, P. Ros, R. Rüger, P. R. T. Schipper, D. Schlüns, H. van Schoot, G. Schreckenbach, J. S. Seldenthuis, M. Seth, J. G. Snijders, M. Solà, M. Stener, M. Swart, D. Swerhone, V. Tognetti, G. te Velde, P. Vernooijs, L. Versluis, L. Visscher, O. Visser, F. Wang, T. A. Wesolowski, E. M. van Wezenbeek, G. Wiesenekker, S. K. Wolff, T. K. Woo and A. L. Yakovlev, ADF 2019.3, SCM, Theoretical Chemistry, Vrije Universiteit, Amsterdam, The Netherlands, http://www.scm.com).
12. (a) D.-C. Sergentu, F. Gendron and J. Autschbach, *Chem. Sci.*, 2018, **9**, 6292-6306; (b) D. Gourier, D. Caurant, T. Arliguie and M. Ephritikhine, *J. Am. Chem. Soc.*, 1998, **120**, 6084-6092.
13. J. P. Perdew, K. Burke and M. Ernzerhof, *Phys. Rev. Lett.*, 1996, **77**, 3865-3868.
14. (a) A. D. Becke, *J. Chem. Phys.*, 1993, **98**, 1372-1377; (b) C. Lee, W. Yang and R. G. Parr, *Physical Review B*, 1988, **37**, 785-789; (c) S. H. Vosko, L. Wilk and M. Nusair, *Can. J. Phys.*, 1980, **58**, 1200-1211.

15. O. V. Gritsenko, P. R. T. Schipper and E. J. Baerends, *Chem. Phys. Lett.*, 1999, **302**, 199-207.
16. B. O. Roos, P. R. Taylor and P. E. M. Sigbahn, *Chem. Phys.*, 1980, **48**, 157-173.
17. (a) G. Li Manni, R. K. Carlson, S. Luo, D. Ma, J. Olsen, D. G. Truhlar and L. Gagliardi, *J. Chem. Theory Comput.*, 2014, **10**, 3669-3680; (b) R. K. Carlson, G. Li Manni, A. L. Sonnenberger, D. G. Truhlar and L. Gagliardi, *J. Chem. Theory Comput.*, 2015, **11**, 82-90.
18. A. Wolf, M. Reiher and B. A. Hess, *J. Chem. Phys.*, 2002, **117**, 9215-9226.
19. (a) B. O. Roos, R. Lindh, P.-Å. Malmqvist, V. Veryazov and P.-O. Widmark, *J. Phys. Chem. A*, 2005, **109**, 6575-6579; (b) B. O. Roos, R. Lindh, P.-Å. Malmqvist, V. Veryazov and P.-O. Widmark, *J. Phys. Chem. A*, 2004, **108**, 2851-2858.
20. P. Å. Malmqvist, B. O. Roos and B. Schimmelpfennig, *Chem. Phys. Lett.*, 2002, **357**, 230-240.
21. G. Ganguly, D.-C. Sergentu and J. Autschbach, *Chem. Eur. J.*, 2020, **26**, 1776-1788.